

Article

Fabrication of Si Nanoparticles@Carbon Fibers Composites from Natural Nanoclay as an Advanced Lithium-Ion Battery Flexible Anode

Sainan Liu ^{1,2}, Qiang Zhang ^{1,2}, Huaming Yang ^{1,2,*} , Dawei Mu ¹, Anqiang Pan ^{3,4} and Shuquan Liang ^{3,4,*}

¹ Centre for Mineral Materials, School of Minerals Processing and Bioengineering, Central South University, Changsha 410083, China; 133101005@csu.edu.cn (S.L.); 175606008@csu.edu.cn (Q.Z.); mudawei@csu.edu.cn (D.M.)

² Hunan Key Lab of Mineral Materials and Application, Central South University, Changsha 410083, China

³ School of Materials Science and Engineering, Central South University, Changsha 410083, China; pananqiang@csu.edu.cn

⁴ Key Lab of Nonferrous Metal Materials Science and Engineering, Ministry of Education, Central South University, Changsha 410083, China

* Correspondence: hmyang@csu.edu.cn (H.Y.); lsq@csu.edu.cn (S.L.); Tel.: +86-731-88830549 (H.Y.)

Received: 20 March 2018; Accepted: 24 April 2018; Published: 27 April 2018



Abstract: In this paper, a cost-effective strategy for fabricating silicon-carbon composites was designed to further improve the electrochemical performance and commercialization prospects of Si anodes for lithium-ion batteries (LIBs). Silicon-carbon fibers (CFs) were prepared by loading Si nanoparticles (SiNPs) on interconnected carbon fibers via an electrospinning technique (SiNPs@CFs). The Si nanoparticles were obtained by the reduction reaction of natural clay minerals. As a flexible anode for LIBs, the SiNPs@CFs anode demonstrated a reversible capacity of 1238.1 mAh·g⁻¹ and a capacity retention of 77% after 300 cycles (in contrast to the second cycle) at a current density of 0.5 A·g⁻¹. With a higher current density of 5.0 A·g⁻¹, the electrode showed a specific capacity of 528.3 mAh·g⁻¹ after 1000 cycles and exhibited a superior rate capability compared to Si nanoparticles. The excellent electrochemical properties were attributed to the construction of flexible electrodes and the composite comprising carbon fibers, which lessened the volume expansion and improved the conductivity of the system.

Keywords: halloysite; silicon; flexible anode; lithium-ion battery

1. Introduction

With the aggravation of the energy crisis and increasing environmental concerns, research on green sustainable energy-storage technology has gained prominence in the energy-storage industry [1–3]. Lithium-ion batteries (LIBs) have attracted growing attention owing to their high energy density, long service life, and environmental benignity [4,5]. In recent years, to enhance the electrochemical performance and expand their application, long-term efforts have been focused on advanced anode materials for LIBs [6–10]. Silicon (Si) has been considered a promising anodic candidate for next-generation LIBs owing to its abundance, high theoretical capacity (~4000 mAh·g⁻¹, approximately 10 times higher than that of current commercial graphite), and low reaction potential with Li ions (<0.4 V versus Li/Li⁺) [11,12]. However, most Si electrodes still suffer from limited cycle performance, which is due to a large volume expansion of >300% resulting from repeated (de)lithiation processes. During the alloying process with Li⁺, the Si anode undergoes a transition from a crystalline state to an amorphous state. The insertion of Li⁺ in the reaction caused the crystal structure of Si to be

severely damaged (the fracture of Si-Si bond and the formation of Si-Li bond) [13]. The expansion and contraction, intensified by Li^+ insertion and extraction, produces a significant amount of shear stress and compressive stress within the material. Meanwhile, the interior of the unit cell cannot provide enough space. Eventually, the stress is not effectively released, resulting in material pulverization and structural failure of the Si electrodes, as well as the shedding of the active material from the current collector [14,15].

Many studies have demonstrated that down-scaling the Si dimensions (in the form of nanoparticles [16], nanotubes [17,18], nanowires [19], nanorods [20], hollow nanospheres [21], etc.), developing new electrolytes and binders [22,23], and doping of Si with conductive buffers (amorphous carbon [24], graphene [25], carbon nanotubes [26], etc.) could be the most effective ways of mitigating the above-mentioned problems. Nanoscale Si materials can effectively balance the volume expansion stress during cycling and maintain the stability of the electrode structure [27,28]. In addition, nano-crystallization can shorten the Li^+ diffusion distance in the active material and increase the ion mobility rate, both of which are conducive to the rate performance of the electrode. Electrospinning is an effective method of obtaining flexible Si-C composites that avoids adding conductive additives or polymer binders [29,30]. Carbon fiber acts as a structural support skeleton and a transport channel for electrons and Li^+ , and its good mechanical properties are conducive to the volume stress release for a Si electrode during repeated cycling. This composite design can prevent the pulverization caused by the Si expansion stress. The formed conductive network increases the overall electrical conductivity of the electrode. Moreover, flexible electrodes can not only partially relieve volume expansions, but can also be applied in the field of wearable electronic devices, which have high commercial prospects [31].

In the Earth's crust, Si is the second-most abundant element, constituting 26.4% of the total mass. It rarely appears as an elementary substance in the natural world, but in the form of complex silicates or silicas, widely found in rocks, gravel, and dust. Extracting Si from natural minerals is highly cost effective. Halloysite, a commonly used natural nanoclay mineral ($\text{Al}_2\text{Si}_2\text{O}_5(\text{OH})_4 \cdot n\text{H}_2\text{O}$), has a layered structure (watery in the interlayer) and inherent tubular morphology [32]. Recently, natural halloysite has shown its effectiveness in several promising applications, such as wastewater treatments [33], nanotube templates [34], and biological drugs containers [35]. Due to the abundance of natural halloysite (the annual global supply exceeds 50,000 T), its price is very inexpensive (approximately \$4/kg) [36]. Hence, extraction of silicon from halloysite nanoclay is very promising.

In this work, high-purity SiO_2 (H- SiO_2) powder was prepared from natural halloysite nanoclay by using selective acid etching. Then, Si nanoparticles (SiNPs) were obtained from as-prepared SiO_2 via magnesiothermic reduction with the assistance of NaCl. Through electrospinning, SiNPs and organic polymer composites were produced. After carbonization, the final product, a flexible Si-C fiber composite (SiNPs@CFs), was collected. As an anode for LIBs, SiNPs@CFs composites could deliver a high reversible capacity of $1238.1 \text{ mAh} \cdot \text{g}^{-1}$ at a rate of $0.5 \text{ A} \cdot \text{g}^{-1}$ after 300 cycles and a capacity of $528.3 \text{ mAh} \cdot \text{g}^{-1}$ at $5 \text{ A} \cdot \text{g}^{-1}$ after 1000 cycles in a voltage range of 0.01–1.2 V (versus Li^+/Li).

2. Materials and Methods

2.1. Material Synthesis

Nanoclay halloysite was directly excavated from Shanxi, China. First, a certain amount of raw materials were dissolved in deionized (DI) water to remove insoluble impurities and soluble ions. Following filtration and washing with DI water, the obtained samples were collected and dried at $60 \text{ }^\circ\text{C}$ under vacuum. Then the next operation is an acid etching process. 5 g of the pre-treated samples was dispersed in 500 mL of hydrochloric acid (2 M). After stirring for 6 h at $100 \text{ }^\circ\text{C}$, Al_2O_3 was removed. After a 3000-rpm centrifugation cycle, the supernatant was collected and washed to neutralize it, and finally dried to produce a white H- SiO_2 remnant.

SiNPs were prepared by magnesiothermic reduction. 1 g of H- SiO_2 , 0.9 g of mg powder, and 10 g of NaCl were placed in a mortar and ground. The powdered mixture was then placed into a quartz

tube furnace and heated to 650 °C for up to 3 h in an argon (Ar) atmosphere with a heating ramp rate of 5 °C·min⁻¹. After cooling to room temperature, the obtained product was dispersed in 2 M HCl for 24 h to remove excess impurities and was washed several times with DI water. The collected SiNPs were dried under vacuum at 60 °C.

The flexible SiNPs@CFs were prepared by electrospinning. 0.2 g of polyacrylonitrile (PAN, Mw = 150,000, Sigma-Aldrich Co., Ltd., St. Louis, MO, USA) and 0.25 g of SiNPs were dissolved in 2 mL of *N,N*-dimethylformide (DMF) and stirred for 24 h at room temperature. The solution was then transferred into a 5 mL syringe with a stainless-steel needle whose specification was 19 G. Then, the needle tip was placed 15 cm from the rolling collector with a high voltage of approximately 9–11 kV. The fibers were collected on an Al foil at 25 °C under a flow rate of 0.12 mm·min⁻¹. The obtained samples were then peeled off and pre-sintered at 250 °C for 90 min, and later sintered at 550 °C in Ar for 2 h.

2.2. Materials Characterization

X-ray diffraction (XRD) of the sample was carried out on a X-ray diffractometer (Rigaku D/max 2500, Rigaku Corporation, Tokyo, Japan) with Cu K α radiation ($\lambda = 1.54178 \text{ \AA}$). The morphologies of the sample were investigated by field-emission scanning electron microscopy (FESEM, Nova NanoSEM 230, 20 kV, FEI Corp., Hillsboro, OR, USA) and high-resolution transmission electron microscopy (HRTEM, Tecnai G2 F20, 200 kV, FEI Corp., Hillsboro, OR, USA). The weight content of CFs in SiNPs@CFs composite was tested on a thermogravimetric analysis under air atmosphere (TGA, NETZSCH STA449F3, Shanghai, China) with a heating rate of 5 °C min⁻¹.

2.3. Electrochemical Characterization

The electrochemical tests of LIBs were carried out in coin-type half-cells (2016 coin cell). The coin cells comprised a cathode (SiNPs@CFs), cut into discs 12 mm in diameter), a polypropylene separator (Celgard 2400), an electrolyte containing a 1 M solution of LiPF₆ in ethylene carbonate/dimethyl carbonate (EC/DMC, 1:1 vol %), and an anode (metallic Li), were assembled in an Ar-filled glove box. The thickness of the obtained fibers was about 30 μm . The mass of the electrode was about 1.1 mg·cm⁻². The calculated specific capacity for the composites anodes is based on the total electrode weight. The working electrode of the Si powder was prepared by dispersing 80 wt % of active materials (Si nanoparticles), 10 wt % of super P conductivity agent and 10 wt % of polyvinylidene fluoride (PVDF) binder in *N*-methyl-2-pyrrolidinone to form a slurry. The slurry was then spread onto copper, dried in a vacuum oven at 80 °C for 12 h and punched into 12 mm size disc electrode (the active material mass loading $\sim 1.2 \text{ mg}\cdot\text{cm}^{-2}$). Galvanostatic charge/discharge tests of the electrodes were conducted in a voltage range 0.01–1.2 V (versus Li⁺/Li) on a battery tester (CT2001A, Land Co., Wuhan, China). Cyclic-voltammetry (CV) measurements were performed on an electrochemical workstation (CHI660C, CH Instruments, Inc., Austin, TX, USA). Electrochemical impedance spectroscopy (EIS) measurements were performed on another electrochemical workstation (IM6ex, ZAHNER-elektrik GmbH & Co. KG, Kronach, Germany) in the frequency range of 100 kHz to 10 m Hz on a cell before cycling.

In the full battery test, the cathode active material was lithium cobalt oxide (Sigma-Aldrich Co., Ltd.), which was mixed with carbon black and polyvinylidene fluoride (70:20:10 mass ratio) in *N*-methyl-2-pyrrolidinone to form a slurry. This slurry was then spread onto an Al foil and dried under vacuum at 80 °C for 12 h to form the working cathode. The mass loading of the cathode was 11 mg·cm⁻². The anode preparation and cell assembly were the same as described above.

3. Results

3.1. XRD Analysis

The XRD patterns of halloysite nanoclay, H-SiO₂ powder, SiNPs, and SiNPs@CFs are shown in Figure 1. As shown, compared with the typical characteristic peak of halloysite nanoclay, a broad peak

at approximately 23° of H-SiO₂ indicates the existence of relatively a pure SiO₂ phase after selective acid etching. To convert H-SiO₂ into Si, magnesiothermic reduction is a viable option, following the chemical reaction $\text{SiO}_2(\text{s}) + 2\text{Mg}(\text{g}) \rightarrow \text{Si}(\text{s}) + 2\text{MgO}(\text{s})$ (exothermic reaction). However, it will lead to the agglomeration of Si particles due to the exothermic process and local overheating. In this case, NaCl was used as a heat absorbent, which kept the reaction temperature below 801°C (the melting point of NaCl) [37]. Moreover, the added NaCl can be easily removed or recycled. It is also conducive to large-scale production owing to its lower reaction costs. Based on this reaction, the peaks at 28.4° , 47.3° , 56.1° , 69.1° , and 76.4° can be assigned to the diffraction planes of (111), (220), (311), (400), and (331) for Si (JCPDS Card No. 27-1402), respectively. No other obvious peaks can be found in the pattern, which means that high-purity Si powder was obtained. After electrospinning and further calcination, there is a wide bulging peak at approximately 26° in the XRD pattern of the as-prepared SiNPs@CFs (see Figure S1 of the Supplementary Materials, ESI†), showing the presence of and confirming the successful synthesis of SiNPs@CFs composites. The CFs content in the SiNPs@CFs composites is about 35 wt % by TG analysis (Figure 1b).

Figure 2 is a schematic of the fabrication process of SiNPs@CFs. Blocky halloysite clay was acidified to obtain white H-SiO₂ powder. After removing Al₂O₃, the sample retained its original tubular morphology, but with a shorter length. After a magnesium reduction process, the as-prepared Si powder shows a claybank color. SiNPs and PAN were homogeneously mixed with DMF as a solvent. After electrospinning and carbonization, flexible SiNPs@CFs were obtained.

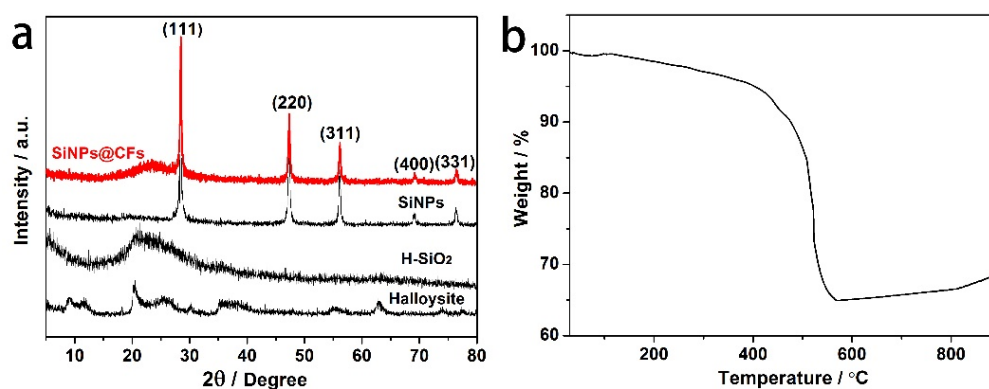


Figure 1. (a) XRD patterns of halloysite, H-SiO₂, SiNPs, and SiNPs@CFs; (b) TGA curve of SiNPs@CFs.

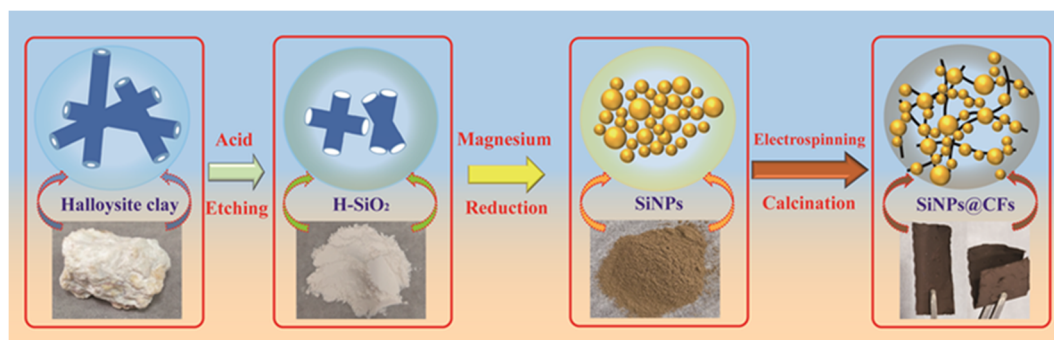


Figure 2. Schematic of SiNPs@CFs preparation process.

3.2. SEM and TEM Analysis

Scanning electron microscope (SEM) and transmission electron microscope (TEM) measurements were carried out to obtain information about the surface morphology and crystal structure of the samples. The original halloysite clay has a nanotube morphology with a length of 1–1.5 μm (Figure 3a),

an average external diameter of 50–75 nm, and an average lumen diameter of 5–15 nm (Figure S2a). After selective acid etching, the obtained H-SiO₂ retains its original tubular morphology, but with a shorter length of 0.2–0.5 μm (Figure S2b). Figure 3c shows a SEM image of the obtained Si particles. As shown, the size is less than 200 nm, while the original tubular morphology cannot be maintained. Figure 3d shows the morphology of SiNPs@CFs. A single carbon fiber was well coated by Si nanoparticles with some local reunification, and the CFs were interlaced with each other. The morphology and microstructure of SiNPs@CFs were further characterized by TEM (Figure 3e) and HRTEM (Figure 3f). Here, large groups of tiny silicon nanoparticles loading on CFs can be observed more clearly. The inset in Figure 3e shows the selected-area electron-diffraction (SAED) pattern, the diffraction rings can be indexed to the (111) and (220) planes of Si. As shown in Figure 3f, the lattice fringes with a spacing of 0.31 nm correspond to the (111) plane of Si. Irregular fringes in the image were also observed, which suggests the existence of carbon.

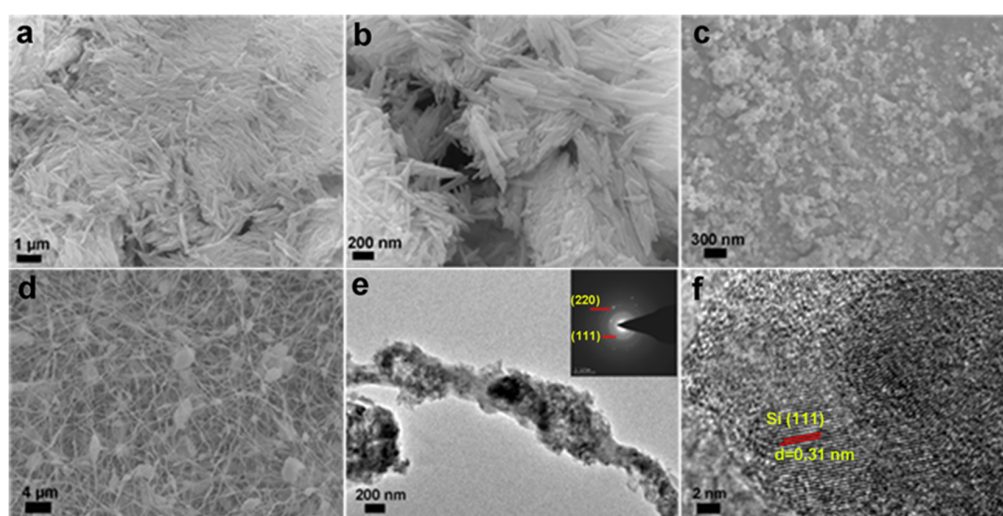


Figure 3. SEM images of (a) original halloysite clay; (b) obtained H-SiO₂ after selective acid etching; (c) SiNPs; (d) SiNPs@CFs; (e) TEM image of SiNPs@CFs with the corresponding SAED pattern (inset e); (f) HRTEM image of SiNPs@CFs.

3.3. Electrochemical Performance Analysis

Figure 4 shows the electrochemical properties of SiNPs@CFs as an anode for LIBs. As shown in Figure 4a, CV measurements were performed in the voltage range 0.01–1.2 V (versus Li⁺/Li) at a scan rate of 0.1 mV·s⁻¹. The first discharge scan shows a broad peak at approximately 1.0–0.02 V that disappeared in subsequent cycles, mainly corresponding to the formation of solid electrolyte interface (SEI) films and the lithiation of crystalline Si into amorphous Li_xSi (Si + xLi → Li_xSi) [38]. The peaks at approximately 0.2 V appearing from the second cycle may be consistent with the lithiation of Si. In charge process, two peaks at 0.32 and 0.47 V can be observed, which is related to the phase transformation from Li_xSi alloy to Si (Li_xSi → Si + xLi). In addition, a peak at approximately 0.02 V on the cathodic branch of cathodic scans may correspond to Li⁺ insertion into CFs (Figure S3a). Figure S4 presents galvanostatic charge/discharge plots of the first, second, 100th, and 300th cycles at a current density of 0.5 A·g⁻¹ over the potential range of 0.01–1.2 V (versus Li⁺/Li). The voltage profile for the first discharge cycle shows a long flat plateau with a capacity of 3097.6 mAh·g⁻¹. The first charge capacity is 1434 mAh·g⁻¹, corresponding to a Coulombic efficiency of 47%, which may result from the formation of SEI films and some irreversible side reactions. The shape of the profiles for the 100th and 300th cycles do not change much, indicating stable electrochemical behavior of the electrode.

The rate performances of SiNPs@CFs and Si powder electrodes for LIBs are displayed in Figure 4b. When cycled at current densities of 0.2, 0.5, 1, 2, and 5 A·g⁻¹, the capacities of SiNPs@CFs are

approximately 1796, 1361, 1020, 794, and 495 $\text{mAh}\cdot\text{g}^{-1}$, respectively. When the current density is reduced back to $0.2\text{ A}\cdot\text{g}^{-1}$, the reversible capacity can recover to $1697\text{ mAh}\cdot\text{g}^{-1}$. In contrast, the Si powder electrode has smaller capacities at the same current density, showing a poor rate performance. Figure 4c shows the cycling performance of the SiNPs@CFs and Si powder electrodes at a current density of $0.5\text{ A}\cdot\text{g}^{-1}$. It is noteworthy that the specific capacities of SiNPs@CFs are calculated based on the total weight of the composite. It is necessary and important to evaluate the capacity contribution of CFs in the SiNPs@CFs composite, shown in Figure S3b. CFs also contribute a certain amount of capacity in the composite electrode. After exhibiting fast capacity fading for the first few cycles, the SiNPs@CFs electrode exhibits a specific capacity of $1238.1\text{ mAh}\cdot\text{g}^{-1}$ at the 300th cycle (Figure 4c), indicating a stable cycling performance. In comparison, the Si powder electrode shows much faster capacity fading, with only a 19% capacity retention after 100 cycles (in contrast to the second cycle). This can be attributed to the unique structure of the SiNPs@CFs composite. The CFs offer a more stable structure as a binder-free support and prevent Si detachment from the current collector, thereby improving the conductivity of the electrode. The long-term cycling performance of the SiNPs@CFs electrode at a higher current density ($5\text{ A}\cdot\text{g}^{-1}$) was also evaluated (Figure 4d) and was found to still exhibit a stable cycle performance for 1000 cycles with a high capacity of $528.3\text{ mAh}\cdot\text{g}^{-1}$.

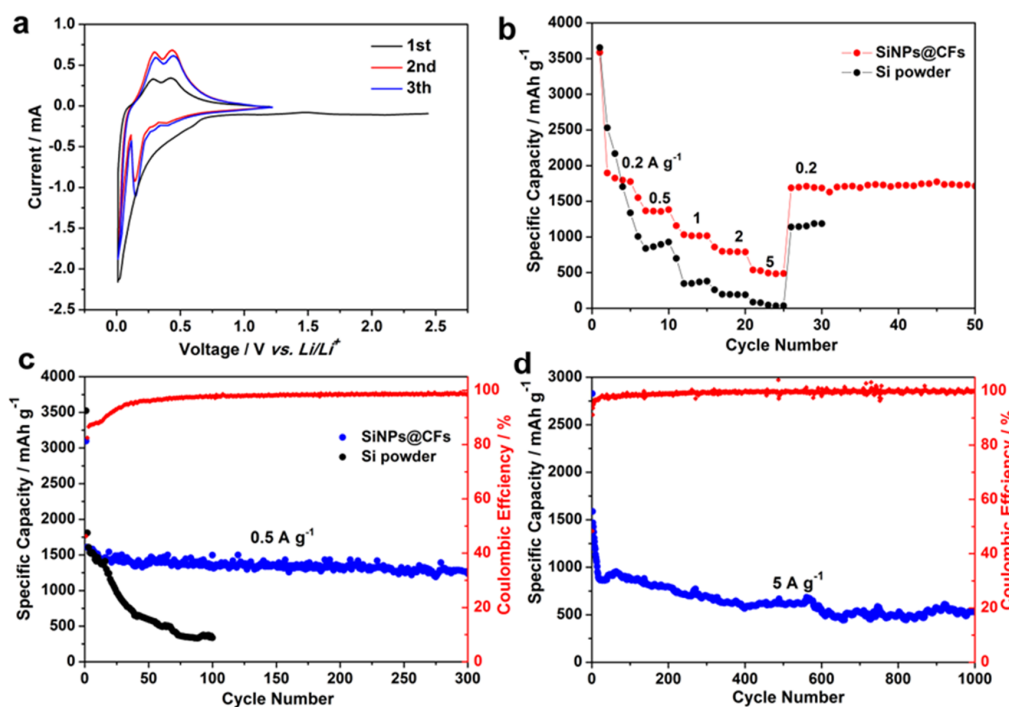


Figure 4. Electrochemical performance of SiNPs@CFs/Li half-cells in the potential range 0.01–1.2 V (vs. Li/Li⁺): (a) CV curves at a sweep rate of $0.1\text{ mV}\cdot\text{s}^{-1}$; (b) rate performance ($0.2\text{--}5\text{ A}\cdot\text{g}^{-1}$) of SiNPs@CFs and pure Si powder; (c) cycling performance of SiNPs@CFs and pure Si powder at $0.5\text{ A}\cdot\text{g}^{-1}$; (d) cycling performance of SiNPs@CFs at $5\text{ A}\cdot\text{g}^{-1}$.

A full battery was assembled by pairing a flexible SiNPs@CFs anode and a lithium cobalt oxide (LCO) cathode (the electrochemical performance of LCO/Li half-cells are shown in Figure S5) to further evaluate the performance of the as-prepared anode at current density of $0.5\text{ A}\cdot\text{g}^{-1}$. Before assembling the full cell, the anode (SiNPs@CFs) had a pre-lithiation process. The purpose of the operation is to consume Li^+ from the external lithium source to form the SEI film. It can ensure that the de-intercalation of Li^+ from the cathode electrode (LCO) will not be wasted in the SEI formation process, and eventually the coulomb efficiency for the first cycle of the full cell could be improved. As shown in Figure 5a, discharge and charge capacities during the first cycle reached 691 and $603.5\text{ mAh}\cdot\text{g}^{-1}$, respectively. It is

worth noting that the discharge capacity is slightly greater than the charge capacity. We think the most possible reason is the presence of stubborn impurities in natural clay minerals. As a result, SiNPs@CFs anode contains some impurities. During the charge and discharge process, these impurities can occur some side reactions with Li^+ and consume some Li^+ , making the discharge capacity higher than the charge capacity. After 100 cycles, the anode discharge capacity remains $469 \text{ mAh}\cdot\text{g}^{-1}$ (Figure 5b). These results further illustrate the promising application of SiNPs@CFs sample for LIB. The cycling results of full-cell without doing pre-lithiation are shown in Figure S6. The full-cell's coulomb efficiency for the first-cycle is lower and the full cell has poor cycle performance.

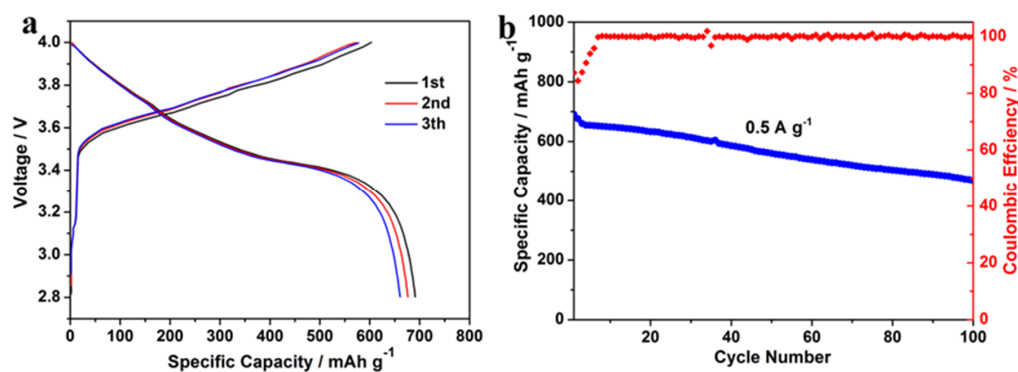


Figure 5. Electrochemical performance of SiNPs@CFs/LCO full cells in the potential range 2.8–4.0 V: (a) Full battery charge/discharge profiles at $0.5 \text{ A}\cdot\text{g}^{-1}$; (b) anode capacity of the full battery for 100 cycles at $0.5 \text{ A}\cdot\text{g}^{-1}$. The capacity is based on the mass of the SiNPs@CFs sample.

4. Discussion

The TEM observation of the electrode after 50 cycles at $0.5 \text{ A}\cdot\text{g}^{-1}$ was performed (in the state of lithium insertion), shown in Figure S7. Figure S7a shows that the nano-particles formed an interconnected structure on the carbon fibers due to the repeated expansion and shrinkage during cycling. Compared to the electrode materials without charge and discharge, obvious volume expansion can be seen. Because the electrode materials (Li_xSi) were in the state of lithium insertion, Figure S7b also displays that Li_xSi is mainly amorphous without obvious crystal plane spacing.

The above electrochemical performance results (for half-cells) of the SiNPs@CFs were compared with previously reported Si anode materials for LIBs (Table S1), and the electrochemical performances of SiNPs@CFs were found to be enhanced. Hence, SiNPs@CFs anodes for LIBs have very good application potential. Zhou et al. [36] reported nanosized Si from natural halloysite clay as an anode for LIBs. In contrast, the unique feature of our work is the preservation of the natural tubular morphology after selective acid treatment, which is a simple and cost-effective method for the preparation of SiO_2 nanotubes that may have many other in-depth applications. Furthermore, this work focuses on flexible Si anodes without a binder and conductive agent, which may be applied to wearable electronic devices in the near future.

To further analyze the improvement in the electrochemical performance, the EIS results of the SiNPs@CFs and Si powder are shown in Figure 6. The semicircle in the high-frequency region indicates the formation of a SEI film and the charge-transfer reaction at the electrode/electrolyte interface, while the straight line appearing at a lower frequency is associated with Li-ion diffusion in the active material. The equivalent-circuit model and numerical values of the equivalent-circuit components for the spectra were investigated (inset of Figure 6 and Table S2), and the charge-transfer resistance of SiNPs@CFs for LIBs was found to be approximately 492.3Ω , which is much lower than that of Si powder (817.6Ω). This confirms that CFs are conducive to improving electrical conductivity and charge-transfer kinetics.

The merits for the superior electrochemical performance of SiNPs@CFs for LIBs are explained as follows: (1) good electronic conductivity of CFs, providing a path for electron transportation; (2) binder-free flexible electrodes, avoiding the use of classical polymer binders (such as PVDF, PAA) is important for reducing the volume expansion; (3) shortened diffusion paths because of nanosized active materials, resulting in rapid charge transport.

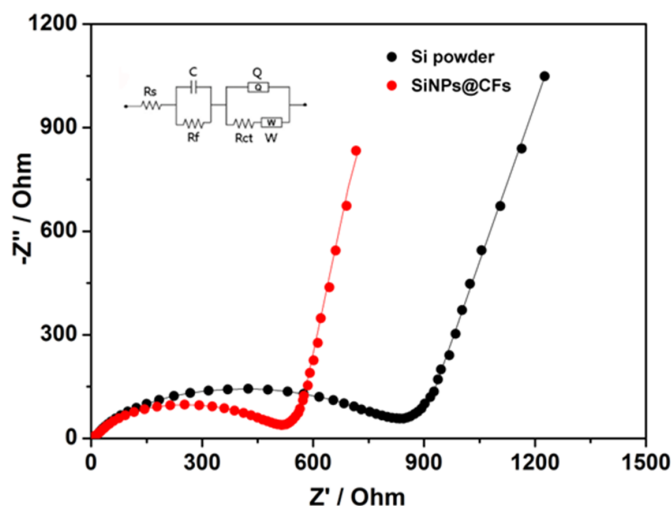


Figure 6. EIS measurements of LIBs employing SiNPs@CFs and pure Si powder as anodes. Inset shows the equivalent circuit of the electrodes.

5. Conclusions

Through a simple and cost-effective method to convert natural halloysite nanoclay into ultrafine SiNPs and by further electrospinning, SiNPs@CFs composite flexible electrodes without conductive agents and binders were prepared. The obtained flexible SiNPs@CFs electrode showed excellent electrochemical performance as LIB anodes, with potentially application in flexible wearable devices.

Supplementary Materials: The following is available online at <http://www.mdpi.com/2075-163X/8/5/180/s1>, Figure S1: XRD pattern of carbon fibers. Figure S2: TEM images of original halloysite clay and the obtained H-SiO₂ after selective acid; Figure S3: Electrochemical performance of CFs/Li half-cells in the potential range of 0.01–3.0 V (vs. Li/Li⁺); Figure S4: The selected discharge–charge curves of SiNPs@CFs/Li half-cells in the potential range of 0.01–1.2 V (vs. Li/Li⁺) at 0.5 A·g^{−1}; Figure S5: Electrochemical performance of LCO/Li half-cells in the potential range of 3.0–4.5 V (vs. Li/Li⁺); Figure S6: Electrochemical performance of SiNPs@CFs/LCO full cells without doing pre-lithiation in the potential range 2.8–4.0 V; Figure S7: TEM and HRTEM image of SiNPs@CFs after 50 cycles at 0.5 A·g^{−1}; Table S1: A comparison of our work with previously reported electrochemical performance of Si anodes for LIBs; Table S2: Numerical values of the equivalent circuit components obtained for the impedance data.

Author Contributions: H.Y. and S.L. (conceiving the project). S.L. (writing initial drafts of the work). H.Y. (writing the final paper). S.L. (designing and performing the experiments, characterizing the samples), Q.Z., D.M. and A.P. (helping in the data analysis). All authors discussed the results and commented on the manuscript.

Acknowledgments: This work was supported by the China Postdoctoral Science Foundation Funded Project (2017M622600), the National Science Fund for distinguished Young Scholars (51225403), the Strategic Priority Research Program of Central South University (ZLXD2017005), the National “Ten Thousand Talents Program” in China, the Hunan Provincial Science and Technology Project (2016RS2004, 2015TP1006), the Changsha Science and Technology Project (kc1702029) and the Hunan Provincial Co-Innovation Centre for Clean and Efficient Utilization of Strategic Metal Mineral Resources (2014-405).

Conflicts of Interest: The authors declare no conflict of interest.

References

1. Hadjipaschalis, I.; Poullikkas, A.; Efthimiou, V. Overview of current and future energy storage technologies for electric power applications. *Renew. Sustain. Energy Rev.* **2009**, *13*, 1513–1522. [[CrossRef](#)]

2. Sternberg, A.; Bardow, A. Power-to-What?—Environmental assessment of energy storage systems. *Energy Environ. Sci.* **2015**, *8*, 389–400. [[CrossRef](#)]
3. Kousksou, T.; Bruel, P.; Jamil, A.; El Rhafiki, T.; Zeraouli, Y. Energy storage: Applications and challenges. *Sol. Energy Mater. Sol. Cells* **2014**, *120*, 59–80. [[CrossRef](#)]
4. Simon, P.; Gogotsi, Y.; Dunn, B. Materials science. Where do batteries end and supercapacitors begin? *Science* **2014**, *343*, 1210–1211. [[CrossRef](#)] [[PubMed](#)]
5. Liu, S.; Zhou, J.; Cai, Z.; Fang, G.; Pan, A.; Liang, S. Nb₂O₅ microstructures: A high-performance anode for lithium ion batteries. *Nanotechnology* **2016**, *27*, 46LT01. [[CrossRef](#)] [[PubMed](#)]
6. Goriparti, S.; Miele, E.; De Angelis, F.; Di Fabrizio, E.; Proietti Zaccaria, R.; Capiglia, C. Review on recent progress of nanostructured anode materials for Li-ion batteries. *J. Power Sources* **2014**, *257*, 421–443. [[CrossRef](#)]
7. Kundu, M.; Karunakaran, G.; Kumari, S.; Minh, N.V.; Kolesnikov, E.; Gorshenkov, M.V.; Kuznetsov, D. One-pot ultrasonic spray pyrolysis mediated hollow mg_{0.25}Cu_{0.25}Zn_{0.5}Fe₂O₄/NiFe₂O₄ nanocomposites: A promising anode material for high-performance lithium-ion battery. *J. Alloys Compd.* **2017**, *725*, 665–672. [[CrossRef](#)]
8. Kundu, M.; Karunakaran, G.; Kolesnikov, E.; Sergeevna, V.E.; Kumari, S.V.; Gorshenkov, M.; Kuznetsov, D. Hollow NiCo₂O₄ nano-spheres obtained by ultrasonic spray pyrolysis method with superior electrochemical performance for lithium-ion batteries and supercapacitors. *J. Ind. Eng. Chem.* **2018**, *59*, 90–98. [[CrossRef](#)]
9. Kundu, M.; Karunakaran, G.; Kolesnikov, E.; Dmitry, A.; Gorshenkov, M.V.; Kuznetsov, D. Hollow (Co_{0.62}Fe_{1.38})FeO₄/NiCo₂O₄ nanoboxes with porous shell synthesized via chemical precipitation: A novel form as a high performance lithium ion battery anode. *Microporous Microporous Mater.* **2017**, *247*, 9–15. [[CrossRef](#)]
10. Kundu, M.; Karunakaran, G.; Minh, N.V.; Kolesnikov, E.; Gorshenkov, M.V.; Kuznetsov, D. Hollow Cu_{0.10}Mg_{0.40}Zn_{0.50}Fe₂O₄/Ca₂Ni₅ nanocomposite: A novel form as anode material in lithium-ion battery. *J. Alloys Compd.* **2017**, *710*, 501–509. [[CrossRef](#)]
11. Li, X.; Gu, M.; Hu, S.; Kennard, R.; Yan, P.; Chen, X.; Wang, C.; Sailor, M.J.; Zhang, J.G.; Liu, J. Mesoporous silicon sponge as an anti-pulverization structure for high-performance lithium-ion battery anodes. *Nat. Commun.* **2014**, *5*, 4105. [[CrossRef](#)] [[PubMed](#)]
12. Wu, H.; Yu, G.; Pan, L.; Liu, N.; McDowell, M.T.; Bao, Z.; Cui, Y. Stable Li-ion battery anodes by in-situ polymerization of conducting hydrogel to conformally coat silicon nanoparticles. *Nat. Commun.* **2013**, *4*, 1943. [[CrossRef](#)] [[PubMed](#)]
13. Zhao, K.; Pharr, M.; Wan, Q.; Wang, W.L.; Kaxiras, E.; Vlassak, J.J.; Suo, Z. Concurrent reaction and plasticity during initial lithiation of crystalline silicon in lithium-ion batteries. *J. Electrochem. Soc.* **2012**, *159*, A238–A243. [[CrossRef](#)]
14. Zhou, X.; Yin, Y.X.; Wan, L.J.; Guo, Y.G. Self-Assembled Nanocomposite of Silicon Nanoparticles Encapsulated in Graphene through Electrostatic Attraction for Lithium-Ion Batteries. *Adv. Energy Mater.* **2012**, *2*, 1086–1090. [[CrossRef](#)]
15. Obrovac, M.N.; Christensen, L.; Le, D.B.; Dahn, J.R. Alloy Design for Lithium-Ion Battery Anodes. *J. Electrochem. Soc.* **2007**, *154*, A849. [[CrossRef](#)]
16. Zhou, X.; Yin, Y.X.; Wan, L.J.; Guo, Y.G. Facile synthesis of silicon nanoparticles inserted into graphene sheets as improved anode materials for lithium-ion batteries. *Chem. Commun.* **2012**, *48*, 2198–2200. [[CrossRef](#)] [[PubMed](#)]
17. Cui, L.F.; Hu, L.; Choi, J.W.; Cui, Y. Light-weight free-standing carbon nanotube-silicon films for anodes of lithium ion batteries. *ACS Nano* **2010**, *4*, 3671–3678. [[CrossRef](#)] [[PubMed](#)]
18. Song, T.; Xia, J.; Lee, J.H.; Lee, D.H.; Kwon, M.S.; Choi, J.M.; Wu, J.; Doo, S.K.; Chang, H.; Park, W.I.; et al. Arrays of sealed silicon nanotubes as anodes for lithium ion batteries. *Nano Lett.* **2010**, *10*, 1710–1716. [[CrossRef](#)] [[PubMed](#)]
19. Chockla, A.M.; Harris, J.T.; Akhavan, V.A.; Bogart, T.D.; Holmberg, V.C.; Steinhagen, C.; Mullins, C.B.; Stevenson, K.J.; Korgel, B.A. Silicon nanowire fabric as a lithium ion battery electrode material. *J. Am. Chem. Soc.* **2011**, *133*, 20914–20921. [[CrossRef](#)] [[PubMed](#)]
20. Zhou, Y.; Jiang, X.; Chen, L.; Yue, J.; Xu, H.; Yang, J.; Qian, Y. Novel mesoporous silicon nanorod as an anode material for lithium ion batteries. *Electrochim. Acta* **2014**, *127*, 252–258. [[CrossRef](#)]

21. Yao, Y.; McDowell, M.T.; Ryu, I.; Wu, H.; Liu, N.; Hu, L.; Nix, W.D.; Cui, Y. Interconnected silicon hollow nanospheres for lithium-ion battery anodes with long cycle life. *Nano Lett.* **2011**, *11*, 2949–2954. [[CrossRef](#)] [[PubMed](#)]
22. Schroder, K.; Alvarado, J.; Yersak, T.A.; Li, J.; Dudney, N.; Webb, L.J.; Meng, Y.S.; Stevenson, K.J. The effect of fluoroethylene carbonate as an additive on the solid electrolyte Interphase on silicon lithium-ion electrodes. *Chem. Mater.* **2015**, *27*, 5531–5542. [[CrossRef](#)]
23. Molina Piper, D.; Evans, T.; Leung, K.; Watkins, T.; Olson, J.; Kim, S.C.; Han, S.S.; Bhat, V.; Oh, K.H.; Buttry, D.A.; et al. Stable silicon-ionic liquid interface for next-generation lithium-ion batteries. *Nat. Commun.* **2015**, *6*, 6230. [[CrossRef](#)] [[PubMed](#)]
24. Yang, J.; Wang, Y.X.; Chou, S.L.; Zhang, R.; Xu, Y.; Fan, J.; Zhang, W.X.; Liu, H.K.; Zhao, D.; Dou, S.X. Yolk-shell silicon-mesoporous carbon anode with compact solid electrolyte interphase film for superior lithium-ion batteries. *Nano Energy* **2015**, *18*, 133–142. [[CrossRef](#)]
25. Chen, S.; Bao, P.; Huang, X.; Sun, B.; Wang, G. Hierarchical 3D mesoporous silicon@graphene nanoarchitectures for lithium ion batteries with superior performance. *Nano Res.* **2013**, *7*, 85–94. [[CrossRef](#)]
26. Fan, Y.; Zhang, Q.; Xiao, Q.; Wang, X.; Huang, K. High performance lithium ion battery anodes based on carbon nanotube–silicon core–shell nanowires with controlled morphology. *Carbon* **2013**, *59*, 264–269. [[CrossRef](#)]
27. Liu, X.H.; Zhong, L.; Huang, S.; Mao, S.X.; Zhu, T.; Huang, J.Y. Size-dependent fracture of silicon nanoparticles during lithiation. *ACS Nano* **2012**, *6*, 1522–1531. [[CrossRef](#)] [[PubMed](#)]
28. Hu, Y.S.; Adelhelm, P.; Smarsly, B.M.; Maier, J. Highly Stable Lithium Storage Performance in a Porous Carbon/Silicon Nanocomposite. *ChemSusChem* **2010**, *3*, 231–235. [[CrossRef](#)] [[PubMed](#)]
29. Hwang, T.H.; Lee, Y.M.; Kong, B.S.; Seo, J.S.; Choi, J.W. Electrospun core-shell fibers for robust silicon nanoparticle-based lithium ion battery anodes. *Nano Lett.* **2012**, *12*, 802–807. [[CrossRef](#)] [[PubMed](#)]
30. Liu, S.; Cai, Z.; Zhou, J.; Zhu, M.; Pan, A.; Liang, S. High-performance sodium-ion batteries and flexible sodium-ion capacitors based on Sb_2X_3 ($X = O, S$)/carbon fiber cloth. *J. Mater. Chem. A* **2017**, *5*, 9169–9176. [[CrossRef](#)]
31. Wang, X.; Lu, X.; Liu, B.; Chen, D.; Tong, Y.; Shen, G. Flexible Energy-Storage Devices: Design Consideration and Recent Progress. *Adv. Mater.* **2014**, *26*, 4763–4782. [[CrossRef](#)] [[PubMed](#)]
32. Ouyang, J.; Mu, D.; Zhang, Y.; Yang, H. Mineralogy and physico-chemical data of two newly discovered halloysite in China and their contrasts with some typical minerals. *Minerals* **2018**, *8*, 108. [[CrossRef](#)]
33. Yu, L.; Wang, H.; Zhang, Y.; Zhang, B.; Liu, J. Recent advances in halloysite nanotube derived composites for water treatment. *Environ. Sci.* **2016**, *3*, 28–44. [[CrossRef](#)]
34. Shu, Z.; Zhang, Y.; Yang, Q.; Yang, H. Halloysite Nanotubes Supported Ag and ZnO Nanoparticles with Synergistically Enhanced Antibacterial Activity. *Nanoscale Res. Lett.* **2017**, *12*, 135. [[CrossRef](#)] [[PubMed](#)]
35. Borrego-Sánchez, A.; Awad, M.; Sainz-Díaz, C. Molecular modeling of adsorption of 5-aminosalicylic acid in the halloysite nanotube. *Minerals* **2018**, *8*, 61. [[CrossRef](#)]
36. Zhou, X.; Wu, L.; Yang, J.; Tang, J.; Xi, L.; Wang, B. Synthesis of nano-sized silicon from natural halloysite clay and its high performance as anode for lithium-ion batteries. *J. Power Sources* **2016**, *324*, 33–40. [[CrossRef](#)]
37. Luo, W.; Wang, X.; Meyers, C.; Wannemacher, N.; Sirisaksoontorn, W.; Lerner, M.M.; Ji, X. Efficient fabrication of nanoporous Si and Si/Ge enabled by a heat scavenger in magnesiothermic reactions. *Sci. Rep.* **2013**, *3*, 2222. [[CrossRef](#)] [[PubMed](#)]
38. Luo, Z.; Xiao, Q.; Lei, G.; Li, Z.; Tang, C. Si nanoparticles/graphene composite membrane for high performance silicon anode in lithium ion batteries. *Carbon* **2016**, *98*, 373–380. [[CrossRef](#)]

